

# Fermi surface topology and negative longitudinal magnetoresistance observed in the semimetal NbAs<sub>2</sub>

Bing Shen,<sup>1</sup> Xiaoyu Deng,<sup>2</sup> Gabriel Kotliar,<sup>2</sup> and Ni Ni<sup>1,\*</sup><sup>1</sup>*Department of Physics and Astronomy and California NanoSystems Institute, University of California, Los Angeles, California 90095, USA*<sup>2</sup>*Department of Physics and Astronomy, Rutgers University, Piscataway, New Jersey 08854, USA*

(Received 4 February 2016; published 9 May 2016)

We report transverse and longitudinal magnetotransport properties of NbAs<sub>2</sub> single crystals. Attributing to the electron-hole compensation, nonsaturating large transverse magnetoresistance reaches up to 8000 at 9 T at 1.8 K with mobility around 1 to 2 m<sup>2</sup> V<sup>-1</sup> S<sup>-1</sup>. We present a thorough study of angular-dependent Shubnikov–de Haas (SdH) quantum oscillations of NbAs<sub>2</sub>. Three distinct oscillation frequencies are identified. First-principles calculations reveal four types of Fermi-surface pockets: electron  $\alpha$  pocket, hole  $\beta$  pocket, hole  $\gamma$  pocket, and small electron  $\delta$  pocket. Although the angular dependence of  $\alpha$ ,  $\beta$ , and  $\delta$  agree well with the SdH data,  $\gamma$  pocket is missing in SdH. Negative longitudinal magnetoresistance is observed which may be linked to novel topological states in this material, although systematic study is necessary to ascertain its origin.

DOI: [10.1103/PhysRevB.93.195119](https://doi.org/10.1103/PhysRevB.93.195119)

## I. INTRODUCTION

Materials with nontrivial topology in their electronic structure often display unusual magnetotransport behavior. Recently large, linear, unsaturating transverse magnetoresistance (TMR) has appeared in Dirac semimetals Cd<sub>3</sub>As<sub>2</sub>, Na<sub>3</sub>Bi, and the Weyl semimetal TaAs family [1–4]. Negative longitudinal magnetoresistance (NLMR) has been discovered in Na<sub>3</sub>Bi, TaAs, and Cd<sub>3</sub>As<sub>2</sub> [2–5]. In these semimetals, electronic structures exhibit accidental band crossings protected by symmetry and linear energy-momentum dispersion near the Fermi level is observed. Due to their nontrivial topological state, exotic phenomena, such as Fermi-arc surface states, negative longitudinal magnetoresistivity (NLMR) have been observed [2,6–9]. Since then, nonmagnetic semimetals with extremely large TMR have re-inspired a lot of research interest because they provide a candidate pool to search for new quantum phases arising from nontrivial topology. NbSb<sub>2</sub> is one of the materials showing TMR up to 1300 at 1.8 K under 9 T. Dirac points were suspected in this material [10,11]. However, no further study has been made to understand its Fermi surface topology and examine whether phenomena caused by nontrivial topology exist. In this paper we study the magnetotransport behavior of NbAs<sub>2</sub> single crystals. Large TMR up to 8000 appears, the Fermi surface topology and NLMR are revealed.

## II. EXPERIMENTAL METHODS

Via chemical vapor transport (CVT) method, single crystals of NbAs<sub>2</sub> were grown using I<sub>2</sub> as the transport agent. The growth took two weeks with the source end at 950° and the sink end at 850°. The growth is endothermic and single crystals were found at the sink end. This is different from the CVT growth of NbAs which is exothermic. The growth habit of the majority of NbAs<sub>2</sub> single crystals were needlelike or bladelikey with long direction along the  $b$  axis. Some of them are platelike

or even three dimensional. The size of the crystals was up to 10 × 8 × 3 mm<sup>3</sup>, which could be shaped along different crystal axes.

Room temperature powder x-ray diffraction has been made using a PANalytical Empyrean x-ray diffractometer employing Cu  $K_{\alpha}$  1.5406 Å radiation. The elemental analysis was made using wavelength dispersive spectroscopy (WDS) in a JEOL JXA-8200 WD/ED combined microanalyzer. Both x-ray diffraction and wavelength dispersive spectroscopy were used to confirm the phase. As representatives, x-ray diffraction patterns and the facets where the x-ray diffractions were made on are plotted in Fig. 1(a) for sample S4 and Fig. 1(b) for sample S2. The (0 0 1) and (2 0 1) planes of S2 were identified and the long shared edge between these two facets is thus determined to be along the  $b$  axis. The top shining facet of S4 was identified to be the (2 0 0) facet and the side plane was identified as the (0 0 1) facet.

Electrical transport measurements were performed using Quantum Design Physical Properties Measurement System (QD PPMS Dynacool). In all measurements we shaped the sample into a thin rectangular bar and adopted standard six-probe configuration. For electrical resistivity ( $\rho_{xx}$ ) and Hall resistivity ( $\rho_{yx}$ ) measurements, magnetic field was swept from –9 to 9 T. The data were then symmetrized to obtain  $\rho_{xx}$  using  $\rho_{xx}(B) = [\rho_{xx}(B) + \rho_{xx}(-B)]/2$  and antisymmetrized to get  $\rho_{yx}$  using  $\rho_{yx}(B) = [\rho_{yx}(B) - \rho_{yx}(-B)]/2$ .

First-principles calculations based on density functional theory (DFT) were carried out to study the electronic structure of NbAs<sub>2</sub>. The full-potential linearized augmented plane-wave method and the generalized gradient approximation of the exchange-correlation potential as implemented in Wien2k package were used [12,13]. Spin-orbit coupling was included in all calculations. The crystallographic structure was taken from Ref. [14], which is described by the centrosymmetric monoclinic  $C12/m1$  space group with  $a = 9.368$  Å,  $b = 33.96$  Å,  $c = 7.799$  Å, and the monoclinic angle between  $a$  axis and  $c$  axis is  $\beta = 119.42^\circ$ . The DFT calculations were performed on a primitive cell with two formula units of NbAs<sub>2</sub>, as well as a conventional cell with four formula units of NbAs<sub>2</sub> [15].

\*Corresponding author: [nini@physics.ucla.edu](mailto:nini@physics.ucla.edu)

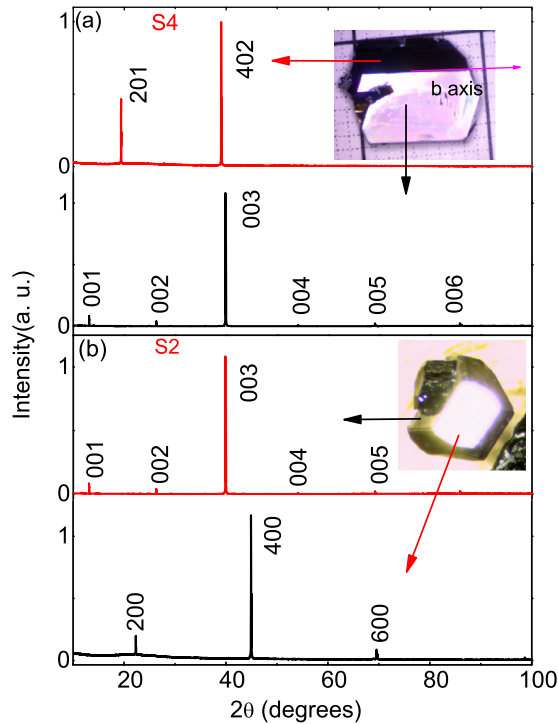


FIG. 1. The x-ray diffraction pattern for (a) sample S4 and (b) sample S2. Insets: Single crystals of S4 (a) and S2 (b) against the 1 mm scale. The size of sample can be up to  $10 \times 8 \times 3 \text{ mm}^3$ .

### III. RESULTS AND DISCUSSION

#### A. Large transverse magnetoresistance and two-band model analysis

Figure 2(a) shows the field dependent TMR, which is defined as  $MR(B) = [\rho_{xx}(B) - \rho_{xx}(0)]/\rho_{xx}(0)$ . TMR shows roughly a  $B^2$  dependence for all samples independent of the current direction. At 1.8 K under 9 T, TMR reaches 230 for S1, 170 for S2, 143 for S3, and 8000 for S4. Figure 2(b) shows the temperature dependent transverse resistivity  $\rho_{xx}$  of NbAs<sub>2</sub> with the current along the  $a$  axis ( $I//a$ ) and the field along the  $b$  axis ( $B//b$ ) for sample S2. Upon decreasing temperature, the zero field  $\rho_{xx}$  decreases with a residual resistivity in the  $\mu\Omega \text{ cm}$  range. As shown in Fig. 2(b), above 2 T, with cooling,  $\rho_{xx}$  decreases first, then increases, and finally saturates at low temperature, resulting in a resistivity minima at  $T_2$  and a flattening below  $T_1$ . With elevated  $B$ ,  $T_2$  moves to higher temperature while  $T_1$  remains almost the same. This field induced upturn of resistivity (so-called transformative turn-on temperature behavior) has been observed in various semimetals with extremely large TMR, such as TaAs, WTe<sub>2</sub>, and its origin is under debate [16–20].

To understand the mechanism of the extremely large TMR data in NbAs<sub>2</sub>, we performed field dependent transverse magnetoresistivity ( $\rho_{xx}$ ) and Hall resistivity ( $\rho_{yx}$ ) measurements at various temperatures for S1 with  $I//b$ . Figure 2(c) shows the representative  $\rho_{xx}$  and  $\rho_{yx}$  data of S1 taken at 10 K. The nonlinear Hall resistivity observed at 10 K indicates a multiband effect in the system. A semiclassical two-band isotropic model is used to analyze the data [18]. We simultaneously fit both  $\rho_{xx}$  and  $\rho_{yx}$  data using  $n, p, \mu$ , and

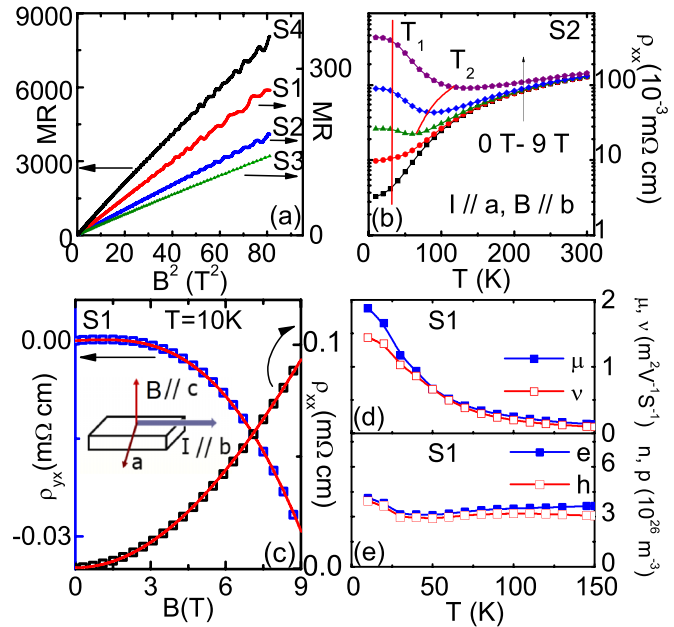


FIG. 2. (a) Transverse magnetoresistance vs  $B^2$  at 1.8 K for sample S1, S2, S3, and S4. (b) Temperature dependent transverse resistivity  $\rho_{xx}$  of sample S2 measured at 0, 1, 2, 4, and 9 T with  $I//a$  and  $B//b$ .  $T_1$  is the temperature where the resistivity flattening occurs and  $T_2$  is the temperature where the minima of  $\rho_{xx}$  appears. (c) Field dependent  $\rho_{xx}$  and Hall resistivity  $\rho_{yx}$  taken at 10 K on S1. The red solid lines are the two-band model fitting curves. Inset: Measurement geometry. (d) and (e) Temperature dependent mobility and carrier density of S1, respectively.

$\nu$  as variables, where  $n(p)$  and  $u(v)$  are the carrier density and mobility of electrons (holes), respectively [15]. The red solid lines in Fig. 2(c) are the fitting curves, showing a very good agreement. Figure 2(d) shows the resulting temperature dependent  $\mu, \nu$  and  $n, p$  for S1. With decreasing temperature, mobility  $\mu$  and  $\nu$  increase drastically and show similar strong temperature dependence. The magnitudes of  $\mu$  and  $\nu$  are comparable to each other for the temperatures from 150 to 10 K with the largest value of  $1\text{--}2 \text{ m}^2 \text{ V}^{-1} \text{ S}^{-1}$  at 10 K. Charge carrier densities  $n$  and  $p$  are also close to each other, but contrary to the strong temperature dependence in  $\mu$  and  $\nu$ , they are almost temperature independent and the magnitude of them is in the  $10^{26} \text{ m}^{-3}$  range. Thus electrons and holes are well compensated in NbAs<sub>2</sub>, which could be responsible for the extremely large TMR. The temperature dependence of mobilities and charge carrier densities resembles the ones in the prototypical semimetal Bi, which also shows extremely large TMR [21,22].

#### B. SdH quantum oscillation and Fermi surface topology

To investigate the Fermi surface topology, we performed angular-dependent magnetotransport measurements at low temperatures. As a representative, Fig. 3 presents our analysis on one set of SdH data taken on S1 at 1.8 K with the geometry shown in the inset of Fig. 3(b) [15]. After subtracting a polynomial background from  $\rho_{xx}$ , obvious quantum oscillations appear above 3 T in the total oscillation (denoted as  $\Delta\rho_{xx}$ ). Figure 3(b) presents the fast Fourier transformation (FFT)

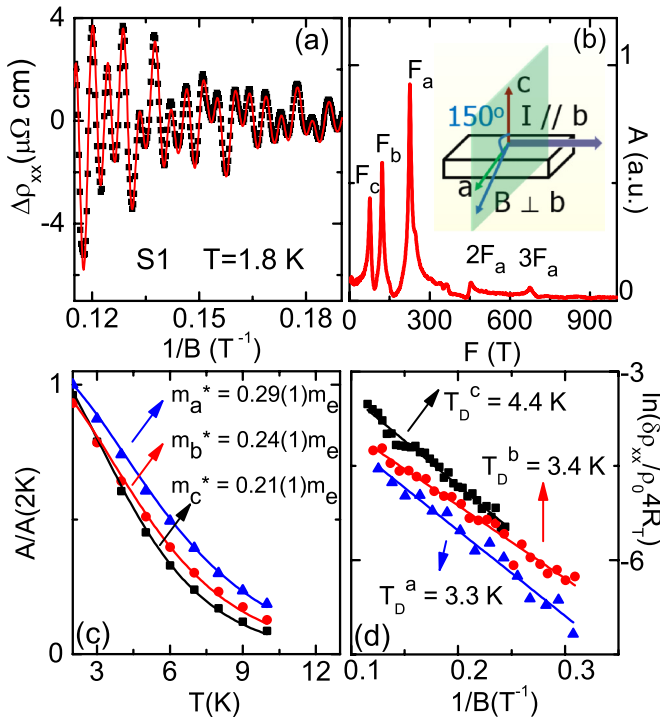


FIG. 3. (a)  $\Delta\rho_{xx}$ , the total oscillation pattern after a polynomial background subtraction vs  $1/B$  measured at 1.8 K with  $1/B$  up to 0.19 ( $\text{T}^{-1}$ ). Experimental data (dots) and reconstructed curve (line). The oscillations observed at  $0.19 \leq 1/B \leq 0.30$  is shown in Fig. S3(a). The measurement geometry is depicted in the inset of (b).  $B$  is  $150^\circ$  away from the  $c$  axis in the  $ac$  plane. (b) The FFT spectrum of  $\Delta\rho_{xx}$  at 1.8 K. Inset: The measurement geometry. (c) The normalized temperature dependent amplitude of the respective oscillation  $\delta\rho_{xx}$  associated with  $F_a$ ,  $F_b$ , and  $F_c$ . Solid line: Fitting. (d) The Dingle plots of the respective  $\delta\rho_{xx}$  associated with  $F_a$ ,  $F_b$ , and  $F_c$ . Solid line: Fitting.  $\rho_0$  is the residual resistivity at 0 T and the reduction factor due to finite temperature  $R_T = \frac{\alpha T m^* / B}{\sinh(\alpha T m^* / B)}$ .

spectrum of  $\Delta\rho_{xx}$ . Three obvious fundamental oscillation frequencies  $F_a$ ,  $F_b$ , and  $F_c$  are identified. The oscillation frequency and the extreme cross section  $S_k$  are related by the Onsager relation  $F = \hbar S_k / 2\pi e$  [23]. Therefore, to obtain information for each Fermi-surface pocket, we used frequency filtering and inverse FFT method to extract the respective oscillation pattern associated with each frequency [15,24] (denoted as  $\delta\rho_{xx}$ ). To check the reliability of this extraction, we reconstructed  $\Delta\rho_{xx}$  by summing respective  $\delta\rho_{xx}$ . Figure 3(a) shows good agreement between the reconstructed (solid line) and experimental oscillation (black dot). The amplitude of each  $\delta\rho_{xx}$  can be expressed by the Lifshitz-Kosevich (LK) formula as  $A(B, T) \propto \frac{\alpha T m^* / B}{\sinh(\alpha T m^* / B)} \exp(-\alpha T_D m^* / B)$  [23]. Here  $\alpha = 2\pi^2 k_B m_e / e\hbar = 14.69 \text{ T/K}$ ,  $m^*$  is the cyclotron effective mass, and  $T_D$  is the Dingle temperature which is related to the single-particle scattering rate  $\tau_s$  by  $T_D = \frac{\hbar}{2\pi k_B \tau_s}$ . At a fixed  $B$ , by extracting the amplitude of the respective  $\delta\rho_{xx}$  at various temperatures, we obtained Fig. 3(c). The fitting results are  $m_a^* = 0.29(1)m_e$ ,  $m_b^* = 0.24(1)m_e$ , and  $m_c^* = 0.21(1)m_e$ . At a fixed  $T$ , by extracting respective  $\delta\rho_{xx}$  at various  $B$  for each frequency, we made Fig. 3(d). The obtained  $T_D$  from fitting is  $T_D^a = 3.3 \text{ K}$ ,  $T_D^b = 3.4 \text{ K}$ , and  $T_D^c = 4.4 \text{ K}$ , resulting in

quantum mobility around  $0.2 \text{ m}^2 \text{ V}^{-1} \text{ S}^{-1}$ . It is common that the quantum mobility is different from the classical mobility obtained from the two-band model fitting of the Hall and TMR data, since the former one is sensitive to all angle scattering while the latter one is insensitive to the small angle scattering. This has been observed in graphene [25], GaAs/Al<sub>x</sub>Ga<sub>1-x</sub>As [26], and Dirac semimetal Ca<sub>3</sub>As<sub>2</sub> [27], etc.

To map out fine structures of the Fermi surface, we rotated  $B$  in the  $ac$  plane of S1 around its  $b$  axis. The rotation geometry is depicted in the inset of Fig. 4(b), with  $\theta$  the rotation angle away from the  $c$  axis. Figure 4(a) shows the 3D map of the FFT spectra for  $\Delta\rho_{xx}$  measured at 1.8 K. Strong angular dependence of the oscillation frequencies  $F_{\text{SdH}}$  is observed and presented in Fig. 4(b). While two other works on NbAs<sub>2</sub> revealed either one or two frequencies with the effective mass ranging from  $0.2m_e$  to  $0.37 m_e$  [28,29], three distinct frequencies  $F_a$ ,  $F_b$ , and  $F_c$  are identified based on Fig. 4(b). Further information can be extracted from Fig. 4(c). It describes the angular-dependent frequency of S2 with  $B$  rotating around the  $a$  axis, where  $\theta$  is the rotation angle away from the  $b$  axis. Four distinct fundamental frequencies  $F_a$ ,  $F_{b1}$ ,  $F_{b2}$ , and  $F_c$  appear in Fig. 4(c). The clear correlation between  $F_{b1}$  and  $F_{b2}$  [Fig. 4(c)] suggests that they arise from the same type of Fermi-surface pocket.

DFT calculations were performed to investigate the Fermi surface topology and compared with the SdH experiments. Calculations using both primitive cell and conventional cell gave consistent results [15]. We found four types of Fermi surfaces in both calculations, which are shown in the reciprocal conventional cell [Figs. 4(d) and 4(e)] [15]: (i) two electron pockets  $\alpha$  near  $X$  point in nearly perfect elliptical shape, (ii) four anisotropic hole pockets  $\beta$  near  $\Gamma$  and away from the BZ boundary, (iii) one hole pocket  $\gamma$  in nearly perfect elliptical shape centered at  $X$  point, and (iv) two small electron pockets  $\delta$  centered close to  $X$  points, which are difficult to see in Fig. 4(d), but better shown in Fig. 4(e). Based on the rotation geometries shown in the inset of Figs. 4(b) and 4(c), we computed the frequency  $F_{\text{DFT}}$  of each pocket using SKEAF [30]. Since the magnitudes of  $F_{\text{DFT}}$  are larger than the ones of  $F_{\text{SdH}}$ , for a better comparison,  $F_{\text{DFT}}/1.78$  is plotted in Figs. 4(b) and 4(c), where  $F_{b1}$  and  $F_{b2}$  originate from two different pairs of  $\beta$  pockets. As a sanity check, at both  $\theta_1 = 150.6^\circ$  [Fig. 3(b)] and  $\theta = 90^\circ$  [Fig. 4(c)],  $B$  is perpendicular to the  $a^*b^*$  plane [Fig. 4(e)], therefore,  $F_{\text{SdH}}$  at these two angles should equal, and so should  $F_{\text{DFT}}$ . This is indeed the case as shown in Figs. 4(b) and 4(c). Table I summarizes the oscillation frequency and effective mass of several special directions obtained from SdH and DFT.

We notice that in both Figs. 4(b) and 4(c) the angular dependence of  $F_a$  matches  $F_\alpha$  well. The maxima of  $F_a$  and  $F_\alpha$  is at  $\theta_1 \sim 60^\circ$ , where  $B//a^*$ . This is consistent with the fact that  $\alpha$  pocket elongates along the normal of the  $a^*b^*$  plane [Fig. 4(e)]. Furthermore, just like  $F_{b1}$  and  $F_{b2}$ , at  $\theta \sim 90^\circ$ ,  $F_{b1}$  intersects with  $F_{b2}$ . Therefore, we assign  $F_{b1}$  and  $F_{b2}$  to the hole pocket  $\beta$ . As a result,  $F_c$  has to be assigned either to the hole  $\gamma$  pocket or to the small electron  $\delta$  pocket. Since the angular dependence and the size of  $F_c$  and  $F_\delta$  are similar, we tentatively assign  $F_c$  to the electron  $\delta$  pocket. We are aware that a DFT work suggests that our  $F_c$  frequency may come from the  $\delta$  pocket [31].

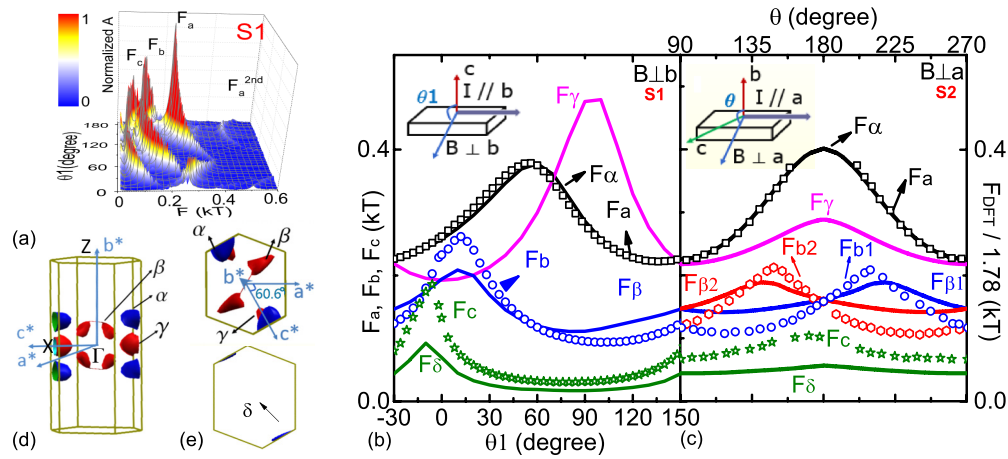


FIG. 4. (a) A 3D plot of the FFT spectra of  $\Delta\rho_{xx}$  taken at 1.8 K for S1. (b) and (c) The angular dependence of oscillation frequencies. Solid lines are the frequency calculated by DFT,  $F_{\text{DFT}}$ , with a scaling factor 1/1.78. Symbols are the frequencies determined by the SdH measurements. Inset of (b): Measurement geometry.  $B$  rotates in the  $ac$  plane and  $\theta_1$  is defined as the rotation angle away from the  $c$  axis. Inset of (c): Measurement geometry.  $B$  rotates around the  $a$  axis and  $\theta$  is defined as the rotation angle away from the  $b$  axis. (d) and (e) The side view and the top view of the Fermi surface, respectively [15].

For the  $\alpha$ ,  $\beta$ , and  $\delta$  pockets, the angular dependencies of  $F_{\text{SdH}}$  and  $F_{\text{DFT}}$  agree well. Although the ratio of the absolute values of  $F_{\text{DFT}}/F_{\text{SdH}}$  varies from around 1 to 1.78, we have to keep in mind that the Fermi-surface pockets only cover a few percent of the whole BZ. For example, a simple estimation of the volume of the  $\alpha$  pocket is around 0.3% of the BZ. Since these pockets are extremely small, possible As vacancies or subtle crystal structure deviation from the one we used in DFT can cause a tiny shift of the relevant bands by a few meV, which could significantly change the absolute sizes of these pockets. It is surprising that we did not detect the corresponding frequency of  $\gamma$  pocket, even if we have observed the  $3F_a$  oscillation [Fig. 3(a)]. The reduction factor of a SdH oscillation can be expressed as  $R_T R_S R_D C$ , where  $R_T$ ,  $R_S$ ,  $R_D$  are the damping factors due to the temperature, spin splitting, and impurity scattering and  $C$  is the curvature factor [23]. Since the effective mass, the size and the shape of  $\alpha$  and  $\gamma$  pockets are very similar in the DFT calculations,  $R_T$ ,  $R_S$ , and  $C$  should be similar for both pockets. Therefore, it is tempting to believe that the missing oscillations associated with the  $\gamma$  pocket may come from larger impurity scattering of this pocket and thus much smaller Dingle damping factor  $R_D$ .

### C. Negative longitudinal magnetoresistance

Another feature we observed is the NLMR. Figure 4 summarizes the measurements. NLMR clearly appears in S2

TABLE I. The comparison of electronic structure parameters of the Fermi-surface pockets in NbAs<sub>2</sub> obtained from experiment and DFT calculations.  $F$  is in kT. \*1 means in the  $a^*b^*$  plane and \*2 means in the  $a^*c^*$  plane.

Pockets	$F_a$	$F_b$	$F_c$	$F_\alpha$	$F_\beta$	$F_\gamma$	$F_\delta$
Frequency*1	0.226	0.122	0.076	0.401	0.261	0.389	0.076
$m^*/m_e^*$ 1	0.29	0.24	0.21	0.29	0.64	0.47	0.25
Frequency*2		0.159	0.102	0.402	0.102	0.290	0.057
$m^*/m_e^*$ 2		0.3	0.26	0.45	0.76	0.71	0.29

with  $B$  rotating in the sample plane and  $I//a$ , where the  $\theta_2$  is defined as the rotation angle away from the  $a$  axis. When  $I//a//B$ , at 1.8 K, with increasing  $B$ , LMR first increases up to 0.5 at 1.5 T, then decreases down to its minimum value of  $-1$  at 1.8 K at 9 T [Fig. 5(a)], resulting in a LMR maximum at 1.5 T. This trend of LMR persists up to much higher temperatures with the LMR maximum moving to higher  $B$ . Up to 9 T, the presence of a MR maxima is still clear at 50 K but is much broadened at 100 K. The overall data pattern

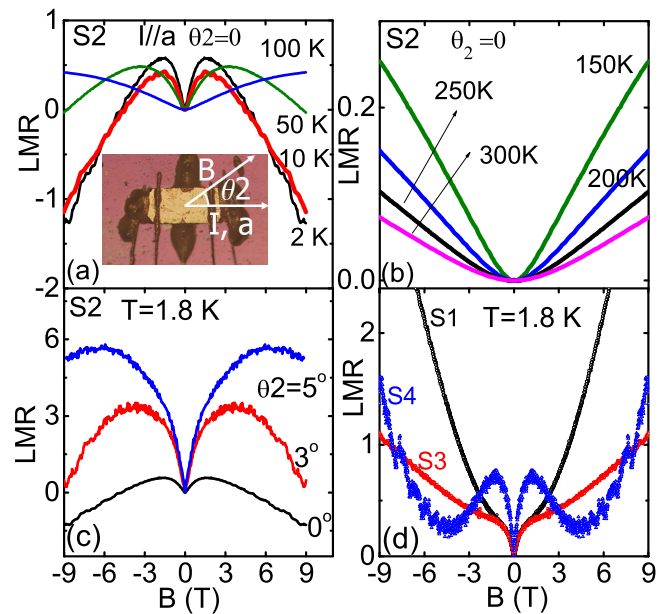


FIG. 5. (a) Field dependent LMR taken on S2 at 1.8, 10, 50, and 100 K with  $B//I//a$ . Inset: Measurement geometry.  $B$  rotates in the sample plane and  $\theta_2$  is defined as the rotation angle away from the  $a$  axis. (b) Field dependent LMR taken on S2 at 150, 200, 250, and 300 K with  $B//I//a$ . (c) Field dependent LMR taken at 1.8 K at different  $\theta_2$ . (d) Field dependent LMR of S1, S3, and S4 at 1.8 K at  $B//I$ .

suggests a competition between two origins, one with positive and the other with negative response to larger  $B$ . With even higher temperatures above 150 K, linear LMR is observed up to 9 T [Fig. 5(b)], which may be a consequence of both responses. This trend of NLMR is robust and persists even when the angle between  $\theta_2$  is  $5^\circ$ , though with a much weaker negative response [Fig. 5(c)]. Figure 5(d) indicates the negative response of S2 is much stronger than the ones in S1, S3, and S4 where S4 has the largest TMR up to 8000 as shown in the inset of Fig. 1(a). Various factors can lead to NLMR [32]. Artifact NLMR can be seen due to asymmetric current flow if the sample size is comparable to the mean free path, poor sample/contact geometry, or the “current jetting” effect due to the large anisotropy of the material [33,34]. We have carefully prepared samples to best avoid these effects. S2 is polished into 0.73 mm long, 0.46 mm wide, and 0.17 mm thick bar [inset of Fig. 5(a)]. The current leads cover the whole area of both edges. The axial anomaly in quasi-two-dimensional materials proposed for the NLMR in PtCoO<sub>2</sub> is mostly unlikely to be the origin of NLMR here since our sample is quite isotropic suggested by both SdH and DFT data (Table I) [35]. Magnetism can cause NLMR, however, no sign of loss of spin scattering appears in our resistivity data and thus impossible to induce such large NLMR. Furthermore, recently it has been proposed that NLMR may occur due to impurity scattering, if the material is in its ultraquantum limit regardless of the band structure [36,37]. However, the negative response clearly shows even at 2 T [Fig. 5(a)], which is far from the ultraquantum limit here. NLMR can also arise from the chiral anomaly if Weyl nodes are created under external field, which is a charge pumping effect between different Weyl

branches [2,4,5,38]. However, careful examination of the band structure and symmetry characterization under field are needed to support this hypothesis. What is more, although great effort has been made to avoid the artifact effect, a systematic study of LMR on samples with different thickness down to tenths of micrometer size is urged to understand the NLMR here [34].

#### IV. CONCLUSION

In conclusion, NbAs<sub>2</sub> is a compensated semimetal with large mobilities, leading to the observed large MR. Three Fermi-surface pockets are identified and their Fermi topology are mapped out both SdH measurements and DFT calculations. Although the oscillations associated with the hole  $\gamma$  pocket are missing, our DFT calculations are overall consistent with the SdH experiment. NLMR exists and further systematic investigation is needed to discern the origin of the observed NLMR.

*Note added in proof.* During the submission of this paper, we noticed several magnetotransport works on TaSb<sub>2</sub>, TaAs<sub>2</sub> [28,29,39–41], and TMR data on NbAs<sub>2</sub> [28,29].

#### ACKNOWLEDGMENTS

Work at UCLA was supported by the U.S. Department of Energy (DOE), Office of Science, Office of Basic Energy Sciences under Award Number DE-SC0011978. Work at Rutgers was supported by the NSF DMREF program under the award NSF DMREF project DMR-1435918. Ni Ni thanks the useful discussion with B. A. Bernevig, A. Coldea, and J. Xiong.

- 
- [1] T. Liang, Q. Gibson, M. N. Ali, M. Liu, R. J. Cava, and N. P. Ong, *Nat. Mater.* **14**, 280 (2015).
- [2] J. Xiong, S. K. Kushwaha, T. Liang, J. W. Krizan, M. Hirschberger, W. Wang, R. J. Cava, and N. P. Ong, *Science* **350**, 413 (2015).
- [3] X. Huang, L. Zhao, Y. Long, P. Wang, D. Chen, Z. Yang, H. Liang, M. Xue, H. Weng, Z. Fang, X. Dai, and G. Chen, *Phys. Rev. X* **5**, 031023 (2015).
- [4] C. Zhang, S.-Y. Xu, I. Belopolski, Z. Yuan, Z. Lin, B. Tong, N. Alidoust, C.-C. Lee, S.-M. Huang, H. Lin, M. Neupane, D. S. Sanchez, H. Zheng, G. Bian, J. Wang, C. Zhang, T. Neupert, M. Z. Hasan, and S. Jia, *Nat. Commun.* **7**, 10735 (2016).
- [5] C.-Z. Li, L. Wang, H. W. Liu, J. Wang, Z.-M. Liao, and D.-P. Yu, *Nat. Commun.* **6**, 10137 (2015).
- [6] Z. Wang, Y. Sun, X.-Q. Chen, C. Franchini, G. Xu, H. Weng, X. Dai, and Z. Fang, *Phys. Rev. B* **85**, 195320 (2012).
- [7] H. Weng, C. Fang, Z. Fang, B. A. Bernevig, and X. Dai, *Phys. Rev. X* **5**, 011029 (2015).
- [8] S.-Y. Xu, I. Belopolski, N. Alidoust, M. Neupane, G. Bian, C. Zhang, R. Sankar, G. Chang, Z. Yuan, C.-C. Lee, S.-M. Huang, H. Zheng, J. Ma, D. S. Sanchez, B. K. Wang, A. Bansil, F.-C. Chou, P. P. Shibayev, H. Lin, S. Jia, and M. Z. Hasan, *Science* **349**, 613 (2015).
- [9] B. Q. Lv, N. Xu, H. M. Weng, J. Z. Ma, P. Richard, X. C. Huang, L. X. Zhao, G. F. Chen, C. E. Matt, F. Bisti, V. N. Strocov, J. Mesot, Z. Fang, X. Dai, T. Qian, M. Shi, and H. Ding, *Nat. Phys.* **11**, 724 (2015).
- [10] K. F. Wang, D. Graf, L. J. Li, L. M. Wang, and C. Petrovic, *Sci. Rep.* **4**, 7328 (2014).
- [11] P. Alemany and S. Alvarez, *Inorg. Chem.* **31**, 3007 (1992).
- [12] P. Blaha, K. Schwarz, G. Madsen, D. Kvasnicka, and J. Luitz, *WIEN2k, An augmented Plane Wave + Local Orbitals Program for Calculating Crystal Properties* (Techn. Universitat Wien, Austria, 2001).
- [13] J. P. Perdew, K. Burke, and M. Ernzerhof, *Phys. Rev. Lett.* **77**, 3865 (1996).
- [14] W. Bensch and W. Heid, *Acta Crystallogr. Sect. C* **51**, 2205 (1995).
- [15] See Supplemental Material at <http://link.aps.org/supplemental/10.1103/PhysRevB.93.195119> for the Brillouin zone folding effects as well as the band structure and Fermi surfaces in the reciprocal primitive cell.
- [16] X. Du, S.-W. Tsai, D. L. Maslov, and A. F. Hebard, *Phys. Rev. Lett.* **94**, 166601 (2005).
- [17] H. Takatsu, J. J. Ishikawa, S. Yonezawa, H. Yoshino, T. Shishidou, T. Oguchi, K. Murata, and Y. Maeno, *Phys. Rev. Lett.* **111**, 056601 (2013).
- [18] M. N. Ali, J. Xiong, S. Flynn, J. Tao, Q. D. Gibson, L. M. Schoop, T. Liang, N. Haldolaarachchige, M. Hirschberger, N. P. Ong, and R. J. Cava, *Nature (London)* **514**, 205 (2014).

- [19] I. Pletikoscic, M. N. Ali, A. V. Fedorov, R. J. Cava, and T. Valla, *Phys. Rev. Lett.* **113**, 216601 (2014).
- [20] Y. L. Wang, L. R. Thoutam, Z. L. Xiao, J. Hu, S. Das, Z. Q. Mao, J. Wei, R. Divan, A. Luican-Mayer, G. W. Crabtree, and W. K. Kwok, *Phys. Rev. B* **92**, 180402 (2015).
- [21] R. Hartman, *Phys. Rev.* **181**, 1070 (1969)
- [22] J. P. Issi, *Aust. J. Phys.* **32**, 585 (1979)
- [23] D. Shoenberg, *Magnetic Oscillations in Metals* (Cambridge University Press, Cambridge, 1984).
- [24] G. Li, Z. Xiang, F. Yu, T. Asaba, B. Lawson, P. Cai, C. Tinsman, A. Berkley, S. Wolgast, Y. S. Eo, Dae-Jeong Kim, C. Kurdak, J. W. Allen, K. Sun, X. H. Chen, Y. Y. Wang, Z. Fisk, and Lu Li, *Science* **346**, 1208 (2014).
- [25] M. Monteverde, C. Ojeda-Aristizabal, R. Weil, K. Bennaceur, M. Ferrier, S. Guéron, C. Glatli, H. Bouchiat, J. N. Fuchs, and D. L. Maslov, *Phys. Rev. Lett.* **104**, 126801 (2010).
- [26] R. G. Mani and J. R. Anderson, *Phys. Rev. B* **37**, 4299 (1988)
- [27] A. Narayanan, M. D. Watson, S. F. Blake, N. Bruyant, L. Drigo, Y. L. Chen, D. Prabhakaran, B. Yan, C. Felser, T. Kong, P. C. Canfield, and A. I. Coldea, *Phys. Rev. Lett.* **114**, 117201 (2015).
- [28] Y.-Y. Wang, Q.-H. Yu, and T.-L. Xia, [arXiv:1601.04239](https://arxiv.org/abs/1601.04239).
- [29] Z. Yuan, H. Lu, Y. Liu, J. Wang, and S. Jia, [arXiv:1601.06482](https://arxiv.org/abs/1601.06482).
- [30] P. M. C. Rourke and S. R. Julian, *Comput. Phys. Commun.* **183**, 324 (2012).
- [31] C. Xu, J. Chen, G.-X. Zhi, Y. Li, J. Dai, and C. Cao, *Phys. Rev. B* **93**, 195106 (2016).
- [32] A. B. Pippard, *Magnetoresistance in Metals* (Cambridge University Press, Cambridge, 1984).
- [33] Y. Ueda and T. Kino, *J. Phys. Soc. Jpn.* **48**, 1601 (1980).
- [34] K. Yoshida, *J. Phys. Soc. Jpn.* **41**, 574 (1976).
- [35] N. Kikugawa, P. Goswami, A. Kiswandhi, E. S. Choi, D. Graf, R. E. Baumbach, J. S. Brooks, K. Sugii, Y. Iida, M. Nishio, S. Uji, T. Terashima, P. M. C. Rourke, N. E. Hussey, H. Takatsu, S. Yonezawa, Y. Maeno, and L. Balicas, *Nature Commun.* **7**, 10903 (2016).
- [36] A. A. Burkov, M. D. Hook, and L. Balents, *Phys. Rev. B* **84**, 235126 (2011).
- [37] P. Goswami, J. H. Pixley, and S. Das Sarma, *Phys. Rev. B* **92**, 075205 (2015).
- [38] H. B. Nielsen and M. Ninomiya, *Phys. Lett. B* **130**, 389 (1983).
- [39] D. Wu, J. Liao, W. Yi, X. Wang, P. Li, H. Weng, Y. Shi, Y. Li, J. Luo, X. Dai, and Z. Fang, *Appl. Phys. Lett.* **108**, 042105 (2016).
- [40] Y. K. Li, L. Li, J. Wang, T. Wang, X. Xu, C. Xi, C. Cao, and J. Dai, [arXiv:1601.02062](https://arxiv.org/abs/1601.02062).
- [41] Y. Luo, R. D. McDonald, P. F. S. Rosa, B. Scott, N. Wakeham, N. J. Ghimire, E. D. Bauer, J. D. Thompson, and F. Ronning, [arXiv:1601.05524](https://arxiv.org/abs/1601.05524).